PAPER

Ceramic–polymer capacitive sensors for tactile/force awareness in harsh environment robotic applications

Smart Mater. Struct. **22** (2013) 125017 (17pp) doi:10.1088/0964-1726/22/12/125017

Ceramic–polymer capacitive sensors for tactile/force awareness in harsh environment robotic applications

Timothy L Weadon[1], **Thomas H Evans**[1,2] **and Edward M Sabolsky**[1]

[1] Department of Mechanical and Aerospace Engineering, WVU, Morgantown, WV, USA
[2] WV Robotic Technology Center, WVU, Fairmont, WV, USA

E-mail: Ed.Sabolsky@mail.wvu.edu

Received 29 April 2013, in final form 27 September 2013
Published 14 November 2013
Online at stacks.iop.org/SMS/22/125017

Abstract
The need for force feedback and spatial awareness of contact in harsh environment applications, such as space servicing, has been unsatisfied due to the inability of current sensor technology to resist environmental effects. In this work, capacitive sensors based on a thick film 0:3 connectivity ceramic:polymer composite structure were evaluated for potential use in future operations within robotic end effectors, withstanding temperatures ranging from −80 °C to 120 °C and forces up to 350 kPa. A thick film design is utilized to allow for ease of embedding, allowing sensors to be implemented into exciting robotic hardware with minimal intrusion, and protecting sensors from electron bombardment, radiation, and point concentrations from metal-on-metal contact. Taguchi design of experiments allows composition variables including sensor thickness, ceramic composition, ceramic particle size, ceramic volume loading, polymer character, modifier character, and the polymer:modifier ratio to be evaluated simultaneously. Dynamic thermal and mechanical loading techniques were implemented to characterize the composite sensors with *in situ* electrical acquisition. Individual composition variables were linked to the sensor magnitude, sensitivity, drift, and hysteresis, showing that the sensor response is optimized with a thickness of single microns, 10 vol% loading of nano-particle ceramics, and high molecular weight polymers with a low content of simple architecture modifiers lacking glass or melting temperatures in the working range.

(Some figures may appear in colour only in the online journal)

1. Introduction

The need for harsh environment force/tactile sensors is becoming increasingly apparent as technology allows for prevalent use of robotics. One such example is on-orbit servicing of satellites, where projections show an annual increase of 11% in new satellite launches [1], and statistics show rapidly increasing on-orbit failures 'to worrying levels' [2]. The effects of on-orbit failures or anomalies has statistically been evaluated to reveal an approximate annual loss of $48 million for typical communications satellites [2]. Advanced robotic operations increase the capability to address common on-orbit decommissioning or unplanned anomalies which can render a satellite as inoperable. Current engineering efforts are in process to prove the capability to robotically refuel, repair, and relocate satellites in need of service [3].

Force feedback and tactile sensing are key technologies to enable remote robotic servicing. To date, harsh environment robotic systems lack the required force and tactile information necessary for preventing damage to hardware by misguided contact, over gripping, or premature contact of robotic end effectors [4]. Commercially available sensor arrays are incompatible for such use, because of electrical and volumetric restraints and environmental conditions [5]. Current robotic systems utilize a range of technologies, including force/torque sensors, strain gauges, motor current

calculations, and flexibility modeling [6]. Although these technologies quantify forces occurring at the end effector, they fail to report any information about contact location, force magnitude, or slipping within the end effector during grappling procedures.

More advanced technologies have recently been proposed for harsh environment applications; these technologies include capacitive proximity sensors (the capaciflector) for contact prediction and embedded spring element sensors for force quantification [5, 7]. The application of the capaciflector sensor was limited, especially in harsh environment robotic applications, due to inadequate levels of resolution. Various mechanical spring sensors experience high drift, and are not designed for complex tooling systems, making integration into existing designs implausible. The most recent advanced tactile technologies discussed in the literature demonstrate the use of silicon-based or micro-electromechanical (MEMs) sensors which are not suitable for high-force, high abrasion, harsh environment applications [8]. While some work with macro-capacitive diaphragms has shown potential in meeting current needs, the low signal output from these sensors is difficult to quantify with onboard electronics, and the sensors are lacking the thorough design needed for identifying and quantifying the source of errors in the response [9]. In order to meet the demands of embedded, harsh environment applications, a number of environmental, mechanical, electrical, and volumetric restraints must be considered. For example, the environmental conditions of space include pressures lower than 10^{-7} Torr and temperatures ranging from $-80\,^{\circ}\mathrm{C}$ to $120\,^{\circ}\mathrm{C}$ (geostationary orbit). The space environment also includes additional complications due to electron/ion bombardment and radiation [10, 11]. In order to meet the contact load requirements, sensors must withstand and measure pressures up to 350 kPa in both static and dynamic modes, and potentially endure direct abrasion with metal contacts, in addition to the other energy bombardment issues described.

Thick film force and tactile sensors are the most commonly fabricated architectures using resistive, piezoelectric, and capacitive activities for sensing. Resistive sensors include strain gauges, piezoresistive polymers and elastomers, and quantum tunneling composites. These sensors have commonly shown drift, hysteresis, creep, and a loss in sensitivity, making them unsuitable for applications requiring accurate force quantification throughout the lifetime of the sensor [12, 13]. In addition to requiring charge amplifiers, piezoelectric sensors have a known drift in the sensor output, requiring additional circuitry when used in static applications. This additional circuitry requires additional power and volume for functionality, which limits their potential use in confined locations [13, 14].

This work proposes the use of capacitive sensor technology for the fabrication of force and tactile sensor arrays, since they exhibit high sensitivity, low drift, reduced temperature dependence, and require low power consumption compared with piezoresistive sensors [15, 16]. The functionality of these sensors is based upon a change in capacitance as a function of a strain which reduces the thickness of the material, as described by the following relation:

$$\Delta C = \frac{\varepsilon_r \varepsilon_0 A}{d_1(1 + 1/\epsilon)}.$$

In this equation, ΔC is the change in capacitance (sensor response), ε_r is the relative permittivity (dielectric constant), ε_0 is the permittivity of free space, A is the area, d_1 is the initial thickness, and ϵ is strain. Capacitive force sensors function by characterizing the relationship between an external pressure and a change in capacitance caused by the introduction of strain (Δd). This relationship can either be experimentally modeled or predicted mathematically using the compressive modulus of the sensor.

Historically, capacitive sensors were fabricated using air as the dielectric material between two electrodes. In an effort to simplify fabrication of the sensors, a thick film design was implemented which allows for simple printing of the electrodes [15, 17]. Additional improvements were made by introducing high dielectric ceramics into the sensor films in order to enhance the capacitance, and thus the sensitivity for small sensor feature sizes [18]. Ceramics are the most prevalently used material in the fabrication of capacitors because of their high dielectric constant. Unfortunately, ceramic materials are not conducive for use in flexible, thick film capacitive sensors due to their high elastic modulus preventing high strain levels. The alternative use of ceramic–polymer composites instead of pure ceramics provides a means for attaining a high dielectric constant while modifying the mechanical compliance of the material for use in capacitive sensor applications. Such a composite should consist of isolated micro/nano-ceramic particles within a polymer matrix to ensure consistent and homogeneous mechanical and electrical properties. This design was pioneered by Newnham *et al*, where connectivity of the microstructure was termed as a 0:3 composite. This notation denotes a filler phase with no interconnectivity in all three dimensions (0-interconnectivity) within a matrix exhibiting three-dimensional interconnectivity (3-interconnectivity) [19].

Most flexible force sensor technologies originated in the biomedical research area and lack the design criteria for use in more extreme temperature environments and cycling conditions. Therefore, many of these sensor platforms are not suitable for applications such as the on-orbit space servicing application previously discussed [16, 18]. The aim of this work is to initiate research on flexible, capacitive force sensors based on a 0:3 composite design for use in harsh environments, specifically aiming the architecture towards a film that may be embedded below a thin metal skin on current space servicing robotic end effector designs. The thickness criteria for these sensors is defined by the need to embed the active sensor material (with patterned interconnect leads) within the end effector in order to protect the sensor from abrasion and energy bombardment. Selection of the active composite materials (ceramic dielectric and organic binder) was purposely chosen to represent a classification of materials that would be representative of those that would be

Table 1. Taguchi design of experiments.

	Thickness	Dielectric material	Particle size	% Dielectric filler	Modifier:binder	Binder	Modifier
Sensor	150/300 μm	PZT/$BaTiO_3$	100 nm/1 μm	10/20 vol%	1:8/1:4	PVDF/PVP[a]	DEGBE/MPTS
A	150	PZT	100 nm	10	1:8	PVDF	DEGBE
B	150	PZT	100 nm	20	1:4	PVP[a]	MPTS
C	150	$BaTiO_3$	1 μm	10	1:8	PVP[a]	MPTS
D	150	$BaTiO_3$	1 μm	20	1:4	PVDF	DEGBE
E	300	PZT	1 μm	10	1:4	PVDF	MPTS
F	300	PZT	1 μm	20	1:8	PVP[a]	DEGBE
G	300	$BaTiO_3$	100 nm	10	1:4	PVP[a]	DEGBE
H	300	$BaTiO_3$	100 nm	20	1:8	PVDF	MPTS

[a] Mixture of 50% PVP and 50% PVDF.

deemed space qualified. These material sets, and the methods and architecture used for the materials, act as a standard baseline for the future use of space qualified materials in future work. Furthermore, the scope of this work included the design and implementation of characterization and testing procedures necessary for qualifying the electromechanical and thermomechanical responses of the sensor materials in the thermal conditions defined by in-orbit robotic operations. Evaluation criteria included the size constraints (for ease of embedding in existing metal parts), electrical, mechanical, and thermal properties affected by the material phase transitions and microstructure variables.

There are a number of variables to be considered in optimizing sensor properties, including sensor thickness, ceramic composition/particle size/volume content, the molecular weight and molecular architecture of polymer and modifier components, and the polymer/modifier ratio. A full two-level design of experiments for evaluating all seven variables would require 2^7 samples, which considering five specimens per sample results in 640 sensors to be characterized. In an effort to maximize efficiency, allowing for an increased number of experimental characterization procedures being performed on each specimen, use of a Taguchi experimental design matrix was implemented. The Taguchi method works by using combinations of results to statistically approximate the influence of a single variable. This is explained in more detail in section 2.1. From this experimental design, an eight-sample matrix (40 specimens) was required to be tested for each characterization method.

2. Experimental details

2.1. Taguchi design of experiments

The Taguchi method was used to design and evaluate the experiments within this work in order to quantify the effects previously described on the sensor performance. The design includes seven unique variables, each having two layers, as shown in table 1. This design is referred to as a 2^7 matrix (or L8), since it requires eight different compositions to evaluate seven variables, with two layers each. While the two-layer design falsely assumes linear trends for all variables considered, it significantly reduces the number of sensor compositions required to complete the testing matrix. This design was strategically selected to decrease testing time, allowing for basic trends to be evaluated for a large number of different testing procedures. The influence of a single variable is approximated by taking the average of all sensors, with each level of the variable being considered. For example, the effect of the sensor thickness is found by considered the average properties of sensors A–D, and that of sensors E–H.

2.2. Materials and processing

As seen in table 1, the eight sensors were labeled A–H for ease of reference. Both the polymer binder and organic modifier materials were used off-the-shelf with no modifications, and were chosen by their differences in molecular weight and molecular architecture. Sensor materials consisted of polyvinylidene fluoride (PVDF, Alfa Aesar, 500 000 g mol^{-1} MW), polyvinylpyrrolidone (PVP, Fisher Scientific, 8000 g mol^{-1} MW), diethylene glycol monobutyl ether (DEGBE, Alfa Aesar, 162.23 g mol^{-1} MW), and 3-methacryloxypropyltrimethoxysilane (MPTS, Alfa Aesar, 248.35 g mol^{-1} MW). The modifiers were chosen for the differences in their molecular architectures, having simple surfactant-like features and complex adhesion promoting features, respectively, as shown in figure 1.

The ceramic Pb(Zr, Ti)O_3 (PZT) with a property of Navy Type II (Piezo Kinetics Inc., PKI-502) and an average particle size of 1 μm was used in this work. The room-temperature dielectric constant of this material was 2000 at 1 kHz. In an effort to attain a second particle size of 100 nm, a portion of this material was attrition milled with 200–400 μm Ce-stabilized zirconia oxide grinding media in an ethanol solution for 10 h. After milling, laser diffraction particle size analysis (Malvern Mastersizer 2000S) was carried out, showing that the desired particle size had been achieved. Scanning electron microscope (SEM) micrographs revealed an increased number of particles in the range of 100 nm, but a population of $\sim$1 μm particles remained after the milling process, as shown in figure 2(a). The ceramic $BaTiO_3$ (BTO, Inframat, Manchester, CT) was used with a particle size of 100 nm and a dielectric constant in the range of 4000 [20]. A portion of material was thermally coarsened to attain a second particle size of 1 μm, using a temperature of 600 °C for 2 h with heating and cooling rates of 3 °C min^{-1}. The resulting material was ball-milled with 6.25 mm cylindrical Mg-doped

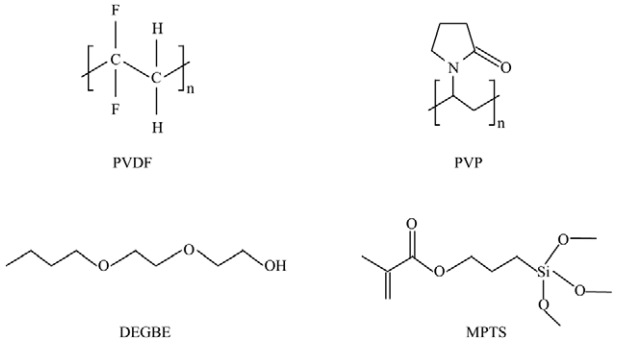

Figure 1. Polymer binder and organic modifier molecular architectures.

ZrO_2 media in an ethanol solution until laser diffraction particle size analysis showed that the desired particle size had been achieved. SEM micrographs showed the increased particle size to be a result of mass agglomeration rather than coarsening, with agglomerations ranging from 1 to 5 μm.

Fabrication of the 0:3 connectivity composite was initiated by creating a solvent solution in a Nalgene® container, consisting of nMP and DMF with a 2:1 ratio by weight. The PZT or BTO particles were added to the solution, and dispersed by sonicating for 1 min at 30% power with a Sonics Vibra-cell sonication wand. The modifier material, DEGBE or MPTS, was added using a pipette. The PVDF or PVP polymer was weighed, then added to the solution and mixed with the unpowered sonication wand. After combining the ingredients, the solution was further sonicated for 2 min at 95% power. Immediately following this step, the solution was poured onto a Mylar film and cast using a micrometer adjustable tape casting blade with a 5 cm doctor blade. The casting thickness was set to 150 μm or 300 μm and a feeler gauge was used to verify the thickness. The resulting film was left at atmospheric conditions for 48 h, and then dried in a vacuum oven at 70 °C and 15 in Hg for 48 h. Compositions E and H were an exception, as they required significantly longer drying times to prevent curling of the films. Electrode films were sputtered on either side using a CVC 610 DC magnetron sputter station with a 5 cm Ag target, a vacuum of 5.0×10^{-6} Torr, and an Ar flow rate of 6 ccm, to achieve a thickness of approximately 500 nm. Sensor specimens were created from the film using an 8 mm diameter punch (unless when otherwise noted).

2.3. Testing schemes

Mechanical testing was performed on the film samples using a TA Instruments Q800 dynamic mechanical analysis (DMA) instrument. Both the static and active clamp surfaces were prepared with copper foil, providing a smooth and full surface for electrical contacts with the silver sputtered sensor faces. A weather-resistant silicone compliance layer was used in series with the active clamp of the DMA to ensure full contact and homogeneous loading. Unless otherwise noted, electrical measurements (capacitance and dielectric loss) were completed using a BK Precision 889B LCR meter at 200 kHz. The LCR leads were passed into the DMA chamber and

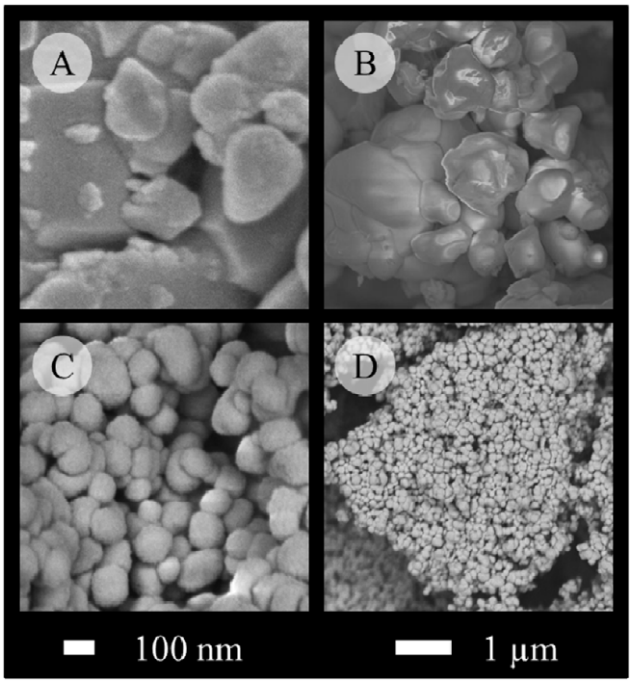

Figure 2. SEM micrographs of the ceramic particles (a) milled PZT, (b) as-received PZT, (c) as-received BTO, (d) calcined BTO.

soldered to silver micro-wires, which were attached to the copper foil creating a flexible conductor to allow *in situ* data acquisition during the dynamic thermomechanical testing scheme. The described testing arrangement is shown in figure 3, with the heating/cooling chamber door open. The testing was initiated by characterizing the room-temperature response to mechanical loading. A series of nine loading steps were used, as shown in figure 4. This procedure was repeated ten times for each specimen, and five specimens were used for each sensor composition (sample).

Since the active mechanism of the sensor response is strain, the stress versus strain diagram can be used to estimate the magnitude and character of the response. The copper pads and compliance layer used for measuring the sensor response were removed to increase the accuracy of the strain measurements. Additionally, bare sensors were tested having no silver coating deposited onto their surface. Because of the finite thickness of the sensors, ten sensors were stacked when testing thin sensors (150 μm tape cast) and five were stacked when testing thicker sensors (300 μm tape cast). Compressive modulus testing was performed using a constant rate of stress of 120 kPa min^{-1}. A total of twenty sequential runs were performed for each of the eight sets of sensors.

Thermomechanical testing was performed in two separate runs, low temperature and high temperature. Low-temperature testing was performed at −80, −40, and 0 °C, dwelling at each temperature for five minutes before performing five loading sequences, as shown in figure 5(a). A load of 40 kPa was maintained throughout the entire load to ensure contact between the leads, and a load of 350 kPa was used to check the sensor response. The specimen was then returned to atmospheric conditions, completing the test sequence, and

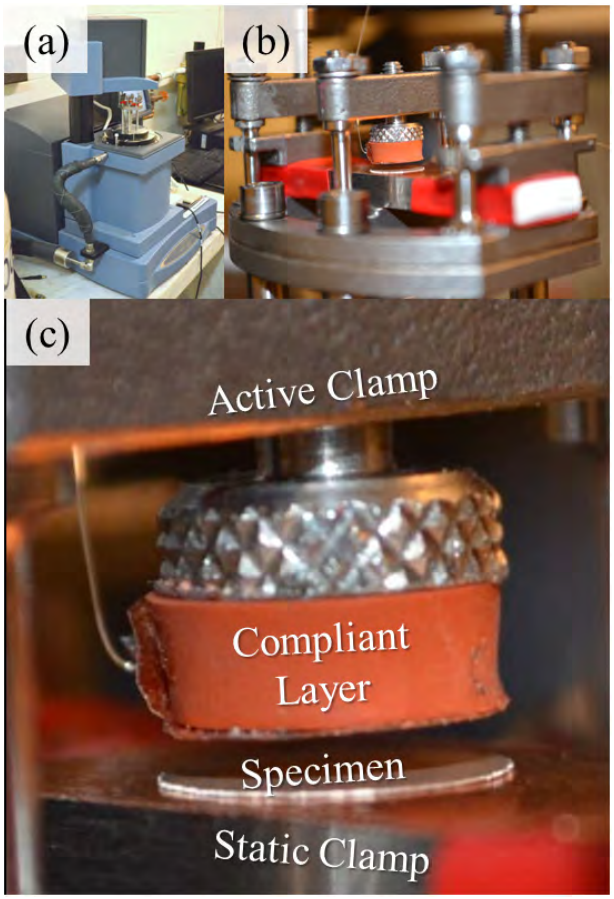

Figure 3. Thermomechanical testing setup: (a) DMA instrument, (b) grip configuration for testing with *in situ* electrical acquisition, (c) compliant layer used to ensure homogeneous pressure distribution.

the testing sequence was repeated twice more. Similarly, high-temperature testing was performed at 40, 80, and 120 °C, dwelling for 10 min before performing the loading sequences (figure 5(b)). The specimens used for thermomechanical testing were chosen from those already used for measuring the capacitive response. This was completed to ensure that materials were preconditioned, allowing for shifting and settling of the microstructure caused by initial mechanical loading.

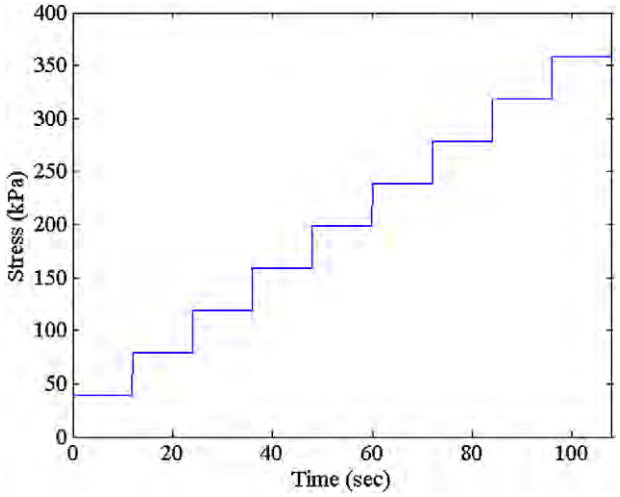

Figure 4. Applied stress versus time schedule used for the sensor response characterization.

The dielectric properties (capacitance and loss tangent) were measured as a function of temperature for the composite materials. Test specimens were increased to a 15 mm diameter to increase the accuracy of the electrical measurements. Testing was performed from −80 to 120 °C in steps of 5 °C using a Delta Design 9023 Environmental Chamber. Electrical measurements were taken using an HP 4284 LCR meter with AC frequencies ranging from 100 Hz to 1 MHz, and the data was recorded using a NI 6008 DAQ card controlled by GADD software.

3. Taguchi testing results

The results from the room-temperature response testing were used to establish the baseline capacitance for the sensors. Since electrical measurements could not be made with an open circuit (since 0 kPa load does not create a contact) the lowest applied force was used as the baseline (40 kPa load). The average of the five specimens for each composition is shown in figure 6.

While all sensors are in a similar range, note that sensor B showed a considerably higher capacitance. Additionally, sensor E has a small variance while sensor C's value was

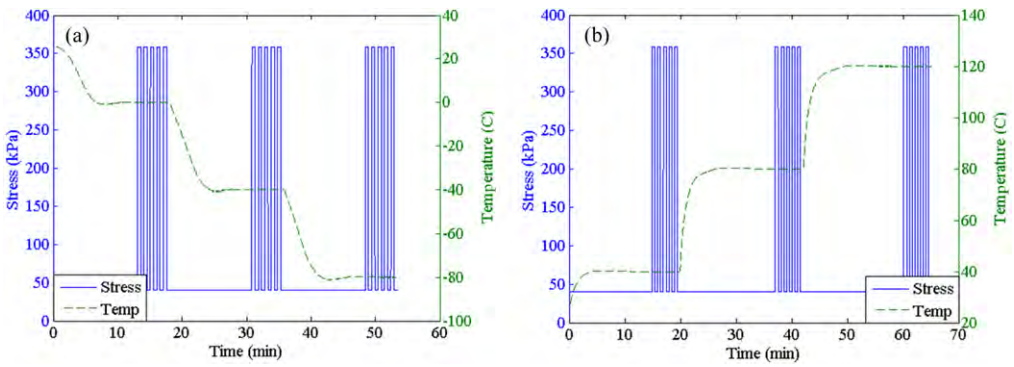

Figure 5. Applied stress versus time schedule used for thermomechanical testing at (a) low temperature and (b) high temperature.

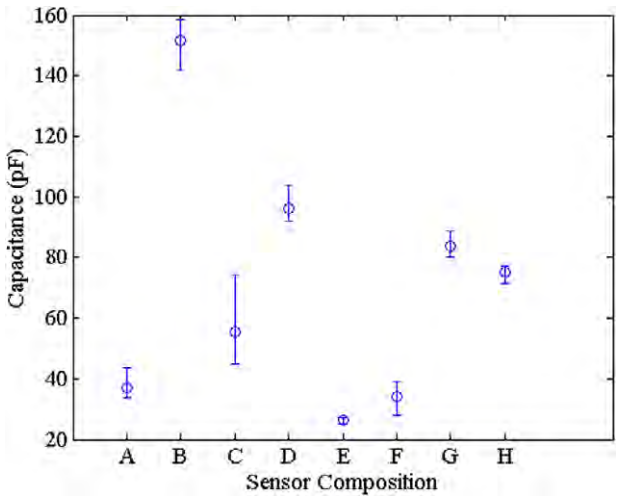

Figure 6. Room-temperature capacitance of minimally loaded (40 kPa) sensor compositions at 200 kHz.

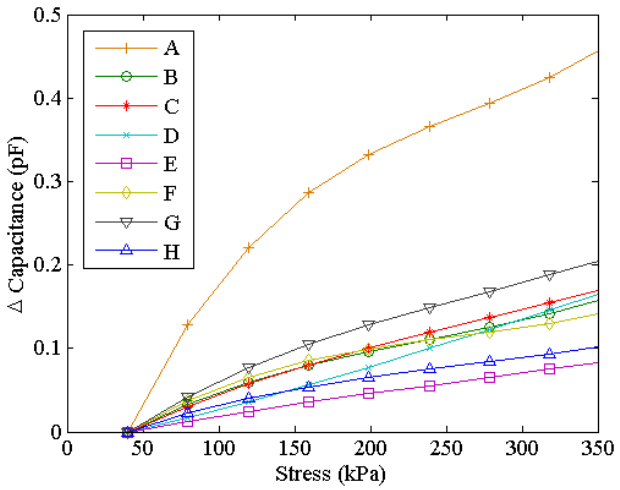

Figure 7. Room-temperature capacitive response of sensor compositions at 200 kHz.

quite large. The response of the sensors is defined as the change in capacitance caused by mechanical loading, and is found by subtracting the baseline capacitance from the full capacitance value while under mechanical loading. These results are plotted in figure 7, where the 40 kPa measurement was found to be 0 pF, since it is considered the baseline.

The response of sensor A far exceeds the others, and sensors E and H lie below the average. It was noted during processing that sensors E and H had substantially longer drying times, and were likely denser than the other sensors. Under closer review it was found that the average coefficient of determination converges to 0.98 for third-order trend lines. This can be seen more easily with sensor A, exhibiting a linear start and a linear tail with a transition between the two linear portions, a trend requiring four points (third order).

Additional testing was performed to give insight into the nonlinear effect of the ceramic content on the sensor response. Ceramic-free sensors were tested as shown in figure 8. Sensor compositions are similar to sensor A, having a 1:8

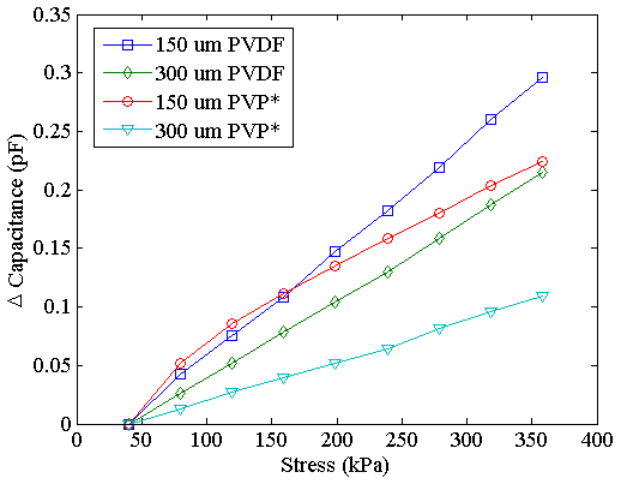

Figure 8. Room-temperature capacitive response of ceramic-free sensor compositions at 200 kHz.

modifier/polymer ratio and using DEGBE as the modifier for all four compositions. Casting thicknesses were either 150 or 300 μm, and the polymer content was either PVDF or 50% PVDF/50% PVP. While the results appear to indicate a higher response without the presence of ceramics, this would be a misinterpretation. The highest response with a purely polymer composition is found with a casting thickness of 150 μm and PVDF. As demonstrated with the sensor A composition, a higher response is attainable with the addition of the ceramic material. This is further described in section 4.3.

Scanning electron microscope (SEM) micrographs show the surface morphology of each sensor composition in figure 9. The SEM shows the porous nature of the films, as well as the large aggregates in material that do not contain PVP (sensors A, D, E, H). The micrographs also show that the ceramic particles are dispersed homogeneously throughout the microstructure, especially for sensors G and H.

The compressive modulus was calculated from the stress versus strain curves in figure 10. Sensor F experienced a compressive modulus much higher than the other sensors, and sensor H was much lower, with Sensors D and E also displaying similar trends. Analogous to the capacitive response to stress, the strain values show a third-order trend. This is not simply a similarity, as the change in capacitance is directly related to the strain. The nonlinear response may be caused by the collapsing of the pore structure within the materials, in addition to the alteration in the intrinsic change in the dielectric properties described in section 4.7. The curves display an initial linear low modulus response and a second-order transitional slope. The response ends with a high linear modulus response.

Traditionally the modulus of a porous material is characterized by the Spriggs equation:

$$E = E_0^{-bp}$$

where E_0 is the non-porous modulus, b is a material constant, and p is the porosity of the material. However, this equation does not efficiently convey information about the sensor properties since the porosity changes as the pores collapse

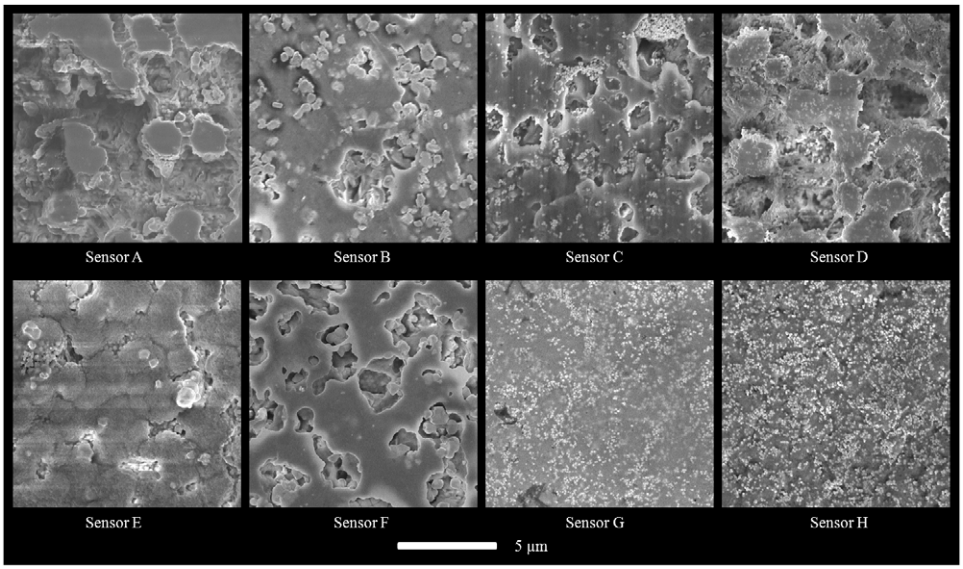

Figure 9. SEM images of the top surface of sensor materials A–H.

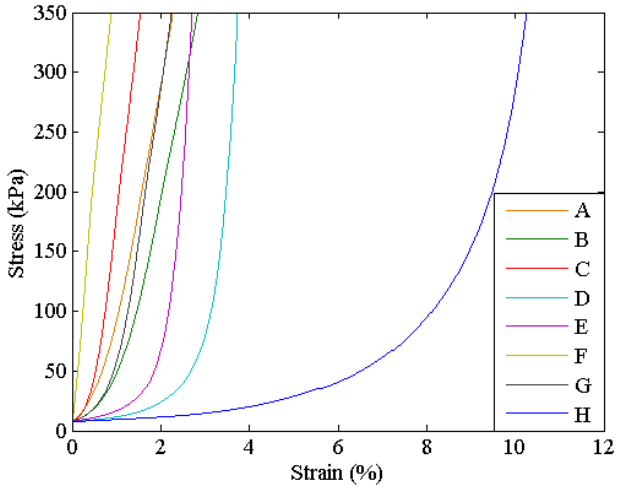

Figure 10. Stress versus strain at room temperature and stressed at a rate of 120 kPa min^{-1} for sensors A–H.

with the introduction of strain. A modified version of this equation could account for such strain:

$$E = E_0^{-b(p_0 - At\varepsilon)}$$

Within this equation, p_0 is the unloaded porosity, A is the surface area of the sensor, t is the original thickness of the sensor, and ε is the strain introduced. This equation assumes that all strain occurs in the porous regions. While this equation more efficiently predicts the modulus of the porous materials, a more simplistic approach is proposed which allows for direct comparison of the initial low modulus region, the transition point, and the compressed high modulus region. The low modulus of each curve was found by fitting a linear trend line from the first point to the second, third, and consecutive points until the coefficient of determination reached a value of 0.98. The high modulus was found in a similar fashion, beginning with the last point and working consecutively backwards. These two linear slopes were then plotted, and a third line was generated to determine the intersection point of interest. The location where this third line intersects with the original curve provides the transition point, giving the stress and strain value where the material transitions from low modulus porous attributes to a higher modulus. This intersection was compared with the first and second derivatives, shown in figure 11, to evaluate the effectiveness of the method.

The thermomechanical testing provided insight into the changes in sensitivity, drift, noise, and sensor hysteresis. The high-temperature testing schedule and the obtained results are shown for sensor A in figure 12, where some of these effects are demonstrated. Sensor A shows excellent sensitivity throughout the temperature range, with negligible noise. A notable shift is observed between the first and second tests, where the trend is not repeated between tests two and three. This shows that settling occurred in the microstructure during the initial thermomechanical load. A smaller drift can be observed in the opposite direction between tests two and three, which represents the thermomechanical drift of the sensor. In addition to the drift, the 120 °C loading sequence shows a time-dependent hysteresis, which can be seen throughout the loading steps and in the initial portion of the unloading steps. While this is most notable during the first test, it persists through tests two and three as well.

The loaded and unloaded responses were averaged for each temperature, and their difference was used to show the response of the sensor. The average response for tests two and three are shown in figure 13 throughout the entire temperature range. Note that the connecting lines do not represent real values, but are intended only to assist the reader with linking the points for each sensor. The response of sensors A and G spike early, and appear to plateau at 80 °C, while the response of sensors E and H rise continually with temperature. The remaining sensors, B–F, experience a small local peak in their response at 40 °C and a large spike at 120 °C.

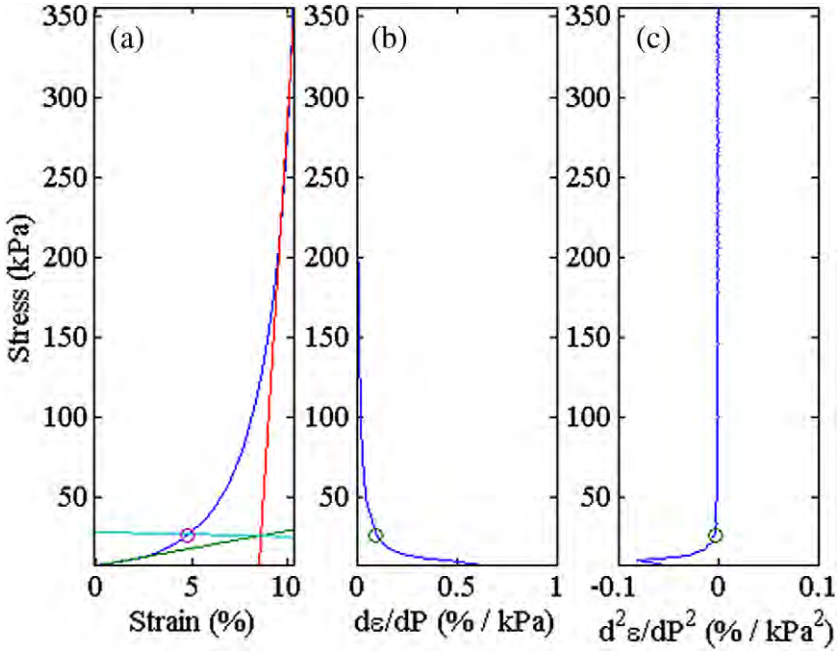

Figure 11. Applied stress versus the % strain and derivatives for determination of the transition point between low strain and high strain deformation of sensor H. Plots shown are: (a) splitting the angle between the two slopes, (b) transition in the first derivative of pressure, and (c) transition in the second derivative of pressure.

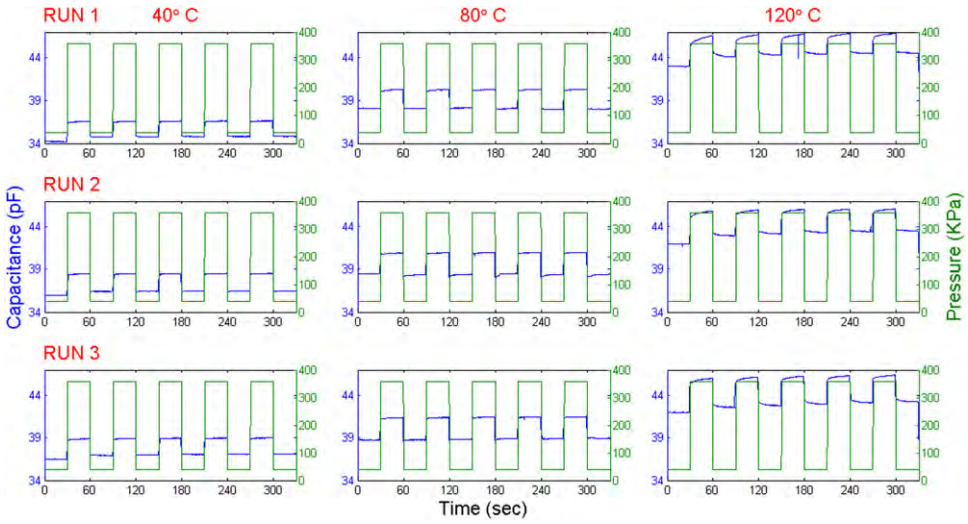

Figure 12. Thermomechanical loading schedule and response of sensor material A.

The intrinsic electrical properties of the composites were also tested as a function of temperature in order to compare against the findings of the thermomechanical testing. The capacitance and dielectric loss tangent values were measured at 200 kHz (same as previous sensor testing) and are shown for the temperature range −80 to 120 °C in figure 14. A distinct peak can be seen in the loss tangent from −40 to 40 °C, and again as the temperature approaches 120 °C. These curves correlate with the nonlinear portion of the capacitive curve in the same temperature ranges.

The capacitance and dielectric loss tangent values are shown across the AC frequency spectrum at room temperature (25 °C) using a logarithmic axis in figure 15. There is a drop in the loss tangent at low frequencies, with a more linear trend beginning between 100 and 200 kHz.

4. Discussion of Taguchi analysis

4.1. Summary of results

The Taguchi analysis is used to relate sensor results to individual variables. In table 2, these results are displayed, showing the influence of each variable and each variable layer. In the Taguchi matrix there were eight different compositions. Since each variable has two layers, there will be four sensors with the first layer, and four sensors with the second layer.

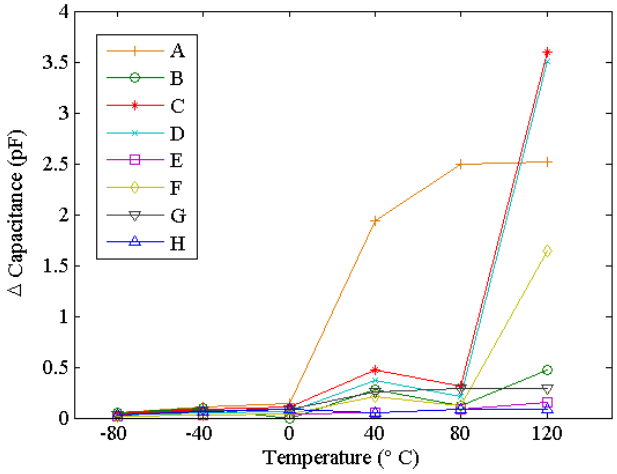

Figure 13. Sensor responses across the full temperature range.

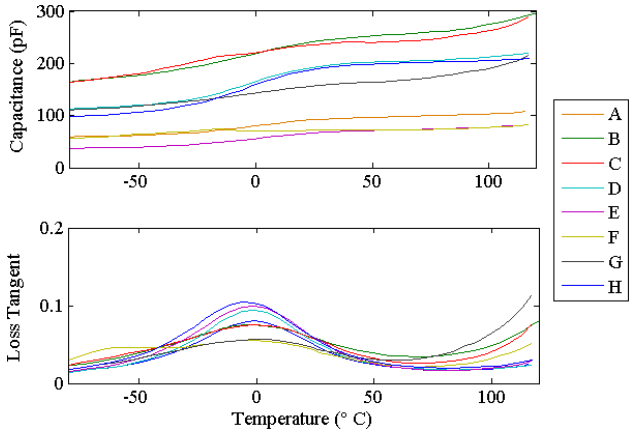

Figure 14. Capacitance and dielectric loss as a function of temperature (measured at 200 Hz) for composite sensor materials A–H.

Taguchi analysis works by showing the average character of the four sensors with layer 1, and the four sensors with layer 2 for each variable. For example, sensors A–D were 150 μm thick and sensors E–H were 300 μm thick. Thus, in the sensor thickness versus capacitive baseline category, the average capacitance of sensors A–D is shown under the 150 μm subhead, and the average capacitance of sensors E–H is shown under the 300 nm subhead.

4.2. Baseline capacitance

As expected from the equation for a capacitor, a higher capacitance was found in compositions that were thinner, contained materials with a higher dielectric constant (BTO), or contained a larger volume percentage of high dielectric materials. Furthermore, Dietze *et al* showed that increasing the ceramic volume content leads to an exponential rise in the capacitance [21, 22]. Compositions with a smaller ceramic particle size were also found to have a higher capacitance, which is consistent with work showing a size-related peak dielectric constant for BTO near a particle size of 70 nm for room-temperature testing [23]. Ferroelectric materials

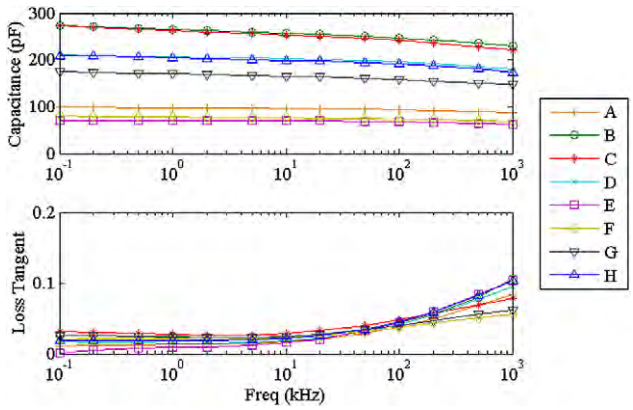

Figure 15. Capacitance and loss tangent as a function of frequency for sensor materials A–H at room temperature.

experience a peak in their dielectric properties at their temperature-induced ferroelectric phase transitions. Materials of a specific particle size will have a set temperature at which they encounter a phase transition in their crystal structure. The phase transition where the material transitions from a ferroelectric to a paraelectric is known as the Curie transition and is characterized by the Curie temperature. However, the Curie temperature of a material is dependent on the particle size, as smaller particles experience this phase transition at lower temperatures. This is known as the ferroelectric size effect [24].

It has been shown that polymers act as linear adsorption isotherms, where polymers with a molecular weight near that of PVP will wrap single surfactant molecules, while high molecular weight polymers, such as PVDF, are found to bind multiple surfactants molecules, creating a complex matrix [25]. Here we find a similar effect in the polymer-filled composites, which are known to create aggregates in the composite microstructure [26]. This occurs as the polymers adsorb to the filler particle (or air bubbles introduced during vigorous mixing) then gradually combine during mixing to create an air- or particle-filled aggregate. The result is small and simple aggregates formed with the PVP compositions, and large, complex aggregates formed with the PVDF compositions. These interactions cause the compositions containing PVP to experience a reduction in internal residual stress over the PVDF. The high molecular weight PVDF molecules also experience recoiling, introducing additional internal residual stresses [27]. These stresses are believed to be normal to the thickness, since they were heavily influenced by the drying process and adhesion of the film to the carrier substrate. Shaw *et al* demonstrated that these internal residual stresses significantly reduce the capacitance of the composite film [28, 29]. There are two primary sources of the converse electrostrictive effect (piezodielectric effect) which decrease the capacitance. The primary sources are the tensile stress occurring normal to the applied current and the compressive stress occurring parallel to the applied current.

The molecular architecture of MPTS is a brush- or star-like form, which restricts efficient organization of these molecules compared to the simpler block copolymer DEGBE.

Table 2. Taguchi results.

	Sensor thickness		Dielectric material		Particle size		Dielectric filler		Polymer organic ratio		Polymer matrix		Organic material	
Character	150 μm	300 μm	PZT	BTO	Small	Large	10 vol%	20 vol%	1:8	1:4	PVDF	PVP[a]	DEGBE	MPTS
Capacitive baseline (pF)	85.060	54.930	62.280	77.710	86.940	53.050	50.760	89.230	50.470	89.520	58.730	81.260	62.790	77.210
Capacitive response (pF)	0.256	0.136	0.216	0.176	0.236	0.156	0.240	0.152	0.231	0.161	0.221	0.171	0.256	0.136
Initial modulus (MPa)	2.550	19.909	21.087	1.372	2.174	20.285	2.591	19.868	21.249	1.210	1.500	20.960	20.943	1.516
Final modulus (MPa)	49.470	105.370	93.990	60.850	48.050	106.790	67.390	87.460	96.450	58.400	39.780	115.060	109.400	45.440
Transition point (kPa)	31.320	51.670	57.900	25.080	33.650	49.330	31.690	51.290	57.650	25.330	29.420	53.570	56.090	26.890
Transition point (%)	0.861	1.742	0.713	1.891	1.709	0.895	0.740	1.864	1.489	1.115	2.124	0.480	0.795	1.808
Response at 120 °C (pF)	1.772	0.545	1.197	1.120	0.844	1.473	1.641	0.676	1.964	0.354	0.814	1.503	1.238	1.079
Response at 80 °C (pF)	0.810	0.145	0.707	0.248	0.747	0.208	0.796	0.159	0.753	0.202	0.743	0.213	0.804	0.151
Response at 40 °C (pF)	0.713	0.142	0.620	0.235	0.627	0.228	0.680	0.176	0.667	0.189	0.551	0.305	0.642	0.214
Response at 0 °C (pF)	0.080	0.062	0.056	0.086	0.079	0.063	0.094	0.048	0.095	0.047	0.083	0.058	0.084	0.058
Response at −40 °C (pF)	0.083	0.049	0.064	0.068	0.084	0.048	0.072	0.060	0.072	0.061	0.062	0.070	0.063	0.069
Response at −80 °C (pF)	0.042	0.021	0.034	0.030	0.041	0.023	0.032	0.032	0.035	0.029	0.030	0.034	0.030	0.033
High-temp mech drift (pF)	1.528	0.701	1.107	1.123	1.648	0.581	1.348	0.882	0.991	1.239	0.792	1.438	1.232	0.998
Low-temp mech drift (pF)	0.121	0.122	0.111	0.132	0.176	0.067	0.124	0.119	0.089	0.154	0.088	0.156	0.144	0.100
Hysteresis at 120 °C (pF)	1.078	0.600	0.727	0.952	0.179	1.499	1.050	0.629	1.585	0.094	0.164	1.515	0.726	0.953
Thermal drift (pF)	102.410	71.880	62.610	111.670	98.630	75.650	80.810	93.470	77.840	96.450	78.040	96.240	71.160	103.120
Cured thickness (μm)	57.23	125.50	88.53	94.20	90.07	92.65	87.22	95.50	99.72	83.00	100.13	82.60	81.08	101.65

[a] Mixture of 50% PVP and 50% PVDF.

Table 3. Composite composition versus average sensor response.

Ceramic (vol%)	Response (pF)
0	0.211
10	0.240
20	0.152

As a result, the MPTS molecules resist packing, thus reducing the consolidation of the composite microstructure during formation. Alternatively, the block-like DEGBE molecules pack more densely, as they are smaller and more flexible. Consequently, films with MPTS exhibited an increased cured film thickness over those with DEGBE. While this effect (being thicker) is expected to result in a lower capacitance for films with MPTS, results were contrary to this prediction. It is believed that compositions containing MPTS may aid in the dispersion of internal residual stress, as the branched molecules provide an increased number of slip-links, which are known to decrease viscosity [30–32].

Increasing the amount of modifier in the matrix increased the capacitance. This is caused by the low molecular weight materials increasing polydispersity in the polymer blend, decreasing viscosity and assisting in the dispersion of internal residual stresses which resulted from the numerous sources described above [33, 34]. Since the internal residual stress reduces the capacitance, sensors with less internal stress experience a higher baseline capacitance [28].

4.3. Room-temperature response

Despite the fact that the thicker sensor materials displayed a larger displacement given a similar strain value, the magnitude of the sensor response is larger in thinner sensors. This effect is expected, since the capacitance of the thinner sensor compositions was higher. Smaller ceramic particles also resulted in a larger response, as they increased the overall capacitance of the material because of their higher dielectric constant (described in section 4.2).

After performing additional testing to quantify the magnitude of the sensor response to a maximum loading of 350 kPa (without the aid of the ceramic materials), it was shown that the relationship between the sensor response and the volume of ceramic content was nonlinear. The average response for 0 vol%, 10 vol%, and 20 vol% content of ceramics is shown in table 3. Note that the 0 vol% average would have been even lower if it had not been maximized by using the 1:8 modifier/polymer ratio and DEGBE as the modifier.

In table 3, it is found that the capacitive response was optimized between 0 vol% and 20 vol% loading of the ceramic in the polymer matrix. It is believed that the sensor response is reduced at the 0 vol% loading of ceramic, because of a reduced dielectric constant of the bulk material. The response was reduced at 20 vol% loading of ceramic because of an increased compressive modulus of the bulk material. Therefore, these results follow the general trend dictated by the idea that a purely polymeric composition would result in a low capacitance, high strain sensor; a purely ceramic composition would result in a high capacitance, low strain sensor.

The sensor materials containing PVDF showed a higher response resulting from a decreased compressive modulus. This is explained in more detail in section 4.4. Since MPTS was found to increase the capacitance and decrease the compressive modulus of the material, it is expected that it will result in a higher capacitive response under mechanical loading. However, this is not the case for room-temperature testing. It is believed that the introduction of internal stresses during mechanical loading decreases the capacitance, as did the introduction of internal residual stresses discussed in section 4.2 [28]. This means that mechanical loading on sensors containing MPTS will simultaneously decrease the capacitance from the introduction of internal stresses while increasing the capacitance from a decrease in thickness. This results in a lower overall change in capacitance as compared with sensors containing DEGBE, which has a higher internal residual stress. Increased modifier content also increased the capacitive response. This effect is caused by an increased polydispersity due to an increased molecular weight distribution of the organic materials, which is widely known to decrease the viscosity of the polymer blend and reduce the modulus of the composite [33, 34].

4.4. Compressive modulus

As expected, the sensor materials with a greater casting thickness were found to have an increased compressive modulus. This is due to an increased level of residual stresses as a result of volume shrinkage during the drying processes. Compositions containing PZT also exhibited a higher compressive modulus. In filler:polymer compositions, changes in the compressive modulus are heavily influenced by surface preparation of the particles. It is believed that the surface chemistry of the materials may be the cause of this effect [35]. The most notable difference between the BTO and PZT used in this work, other than the chemical composition, is that hydrothermal synthesis of BTO gives a surface with high hydroxyl group adsorption, and the spray drying of the PZT gives a surface known to have ammonium group adsorption [36, 37]. Additional surface chemistry characterization should be carried out as a part of future work.

Larger particles were found to increase the compressive modulus, which is contrary to traditional composite trends [38]. However, it has been shown that particles in the range of those used for this testing matrix have similar effects on the modulus despite their size differences [39]. Additionally, it has been demonstrated that differences in the polymer morphology surrounding the particles can have a significant effect on the modulus [35]. This may have contributed to the unpredicted results described. As is expected from use of the rule of mixtures and shown in experimental results, an increased volume of ceramic particles gives rise to the modulus [40, 41]

$$E_c = fE_f + (1-f)E_m.$$

Here E is the elastic modulus, subscripts c, f, and m stand for composite, filler, and matrix, respectively, and f is the volume fraction of the filler material.

At room temperature, the sensor compositions with a PVP polymer matrix experienced a higher modulus. This was caused by PVP being below its glass transition temperature (175 °C) and the PVDF being above its glass transition temperature (about 35 °C) [42, 43]. The modulus of compositions containing PVP may have also been higher, as the microstructure is predicted to be more rigid and less porous. Additionally, PVDF solutions are shown to create large air-filled aggregates when air is introduced by aggressive processes of the composition [26, 44]. These large, air-filled, aggregates likely form during mixing and sonic dispersion of the solution, introducing additional air pockets into an already porous structure, further decreasing the modulus.

As previously described, the simple molecular architecture of DEGBE led to an increased packing of the microstructure, resulting in a thinner, denser bulk material. The increased density led to a rise in the residual stresses, which further increases the compressive modulus. As described in section 4.2, increasing the modifier content will decrease the viscosity of the polymer matrix. This causes the elastic modulus to decrease.

4.5. Thermomechanical response

The completed measurements showed that changing the sensor thickness, ceramic volume loading, and polymer/modifier ratio altered the capacitive response similarly throughout the thermomechanical loading schedule over the entire temperature range (−80 to 120 °C). Since the details of these effects have already been summarized in the room-temperature response section, they will not be further discussed here. The effects of PZT and BTO on the sensor response are complex. The sensor response (ΔC) for an applied load of 350 kPa is shown at different temperatures in figure 16. This figure shows transition points for both materials near 40 °C and above 120 °C.

This complex relationship can be best described by first outlining the Curie temperatures for the ceramic materials. As the materials approach their Curie temperature, the capacitance spikes, in turn giving higher responses from the sensors [45]. Both the small and large PZT particles have a Curie temperature of 390 °C, which is far outside the range of this application [46, 47]. In contrast, BTO particles have a number of transition temperatures in the working range. BTO particles which are 200 nm or larger have a Curie temperature just above 120 °C, identified by a phase transition from the paraelectric cubic phase to ferroelectric tetragonal phase when reducing the temperature to below 120 °C. As the temperature is further reduced below the Curie temperature, the dielectric constant of the particles quickly drops, with the exception of two spikes occurring at additional phase transitions, from the tetragonal to orthorhombic near 20 °C, and from the orthorhombic to rhombohedral phase near −75 °C [48, 49]. Unlike the polymer matrix, the sub-micron BTO particles experience a rise in permittivity

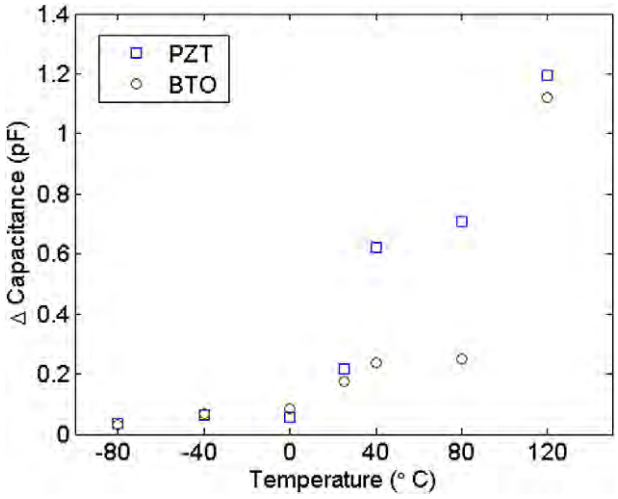

Figure 16. Capacitance response (ΔC) as a function of temperature for sensor materials containing PZT (average of sensors A, B, E, F) and BTO (average of sensors C, D, G, H).

correlating with increased internal stress [50–53]. This was shown computationally by Buessem *et al* using internal stress models and thermodynamic theory, and was further confirmed using x-ray diffraction (XRD), suggesting that the change in permittivity is accounted for as internal stresses force the crystal structure back towards the cubic phase.

While these phase transitions are common to BTO of all sizes, the temperature of their occurrence is significantly affected by the aforementioned size effect for particles under 200 nm. For example, particles of 100 nm in size experience a Curie temperature (transition to the tetragonal phase) in the region of 40 °C [20, 54]. This introduces further transitions in the dielectric constant into the composites. These capacitive spikes account for the aforementioned trends, where BTO experienced a spike in the region of 40 °C, and another approaching just above 120 °C. The cause of the nonlinear regions found with PZT are unaccounted for, though it is believed they are related to stress properties in the thin film [55].

As expected, the thermomechanical loading of the composites showed a strong dependence on the glass transition temperature of the polymer matrix materials. In the range 0 to 80 °C, a greater response was found with the PVDF, where the PVP had a higher response at temperatures of −40 °C and below, and at 120 °C. The exchange between 0 °C and 40 °C is accounted for as the PVDF reaches its glass transition temperature in the region of −35 °C, giving a quick rise to its modulus [43]. Similarly, PVP becomes more sensitive at the higher temperature of 120 °C as it approaches its glass transition temperature of 175 °C [42].

As explained in section 4.3, sensor compositions containing DEGBE had a greater response at room and higher temperatures. At temperatures of −40 °C and lower, compositions containing MPTS showed an increased response. It is believed that the modifier material passes its glass transition temperature at this point, where the material becomes more brittle and begins to micro-crack

under mechanical loading. Upon molecular separation of the MPTS molecules from the binder polymer, slip lines are introduced. This allows internal stresses to be released and reduces the rigidity of the material, leading to a lower elastic modulus. This is the source of the increased capacitance observed with MPTS at low temperatures.

4.6. Rate-dependent hysteresis at 120 °C

In their amorphous state, all polymers exhibit some amount of viscoelastic character. However, since viscoelasticity is defined by time-dependent behavior and is quantified by the dynamic modulus, quasi-static loading gives the appearance of a fully elastic modulus, as was seen for testing at 80 °C or lower in this work. In contrast, a large rate-dependent hysteresis was found during mechanical loading at 120 °C, indicating that the loading scheme was no longer quasi-static. This indicates that the loading rate schedule was occurring rapid enough to affect the stress versus strain relationship. Since the velocity of the loading scheme was not altered, there must have been a transition in the composite material causing an increase in the viscous behavior of the viscoelastic polymer matrix.

Viscoelastic behavior has been shown to depend on three primary variables affecting molecular and sub-molecular cooperative motion of the polymer chains. These are the length of the polymers (represented by the average molecular weight), the mobility of the polymers, and sub-molecule/intermolecule interactions [30]. Molecules that are longer and more flexible will show an increase in slip-links and exhibit more viscous behavior [31, 32]. When thermal loading is applied to the amorphous polymer matrix, the additional energy introduced causes an increase in mobility and interactivity [56].

Thin films ($t < 80$ nm) have been shown by Dalnoki-Veress *et al* to exhibit a reduced glass transition temperature as the film thickness is decreased, which translates to an increased hysteresis for thinner films as higher mobility is achieved with lower energy. However, this trend is limited to thin films and does not extend to the thick films discussed in this work [32]. Rather, this work showed that hysteresis was reduced with an increase in the film thickness. Thick films ($t > 10$ μm) show an increased internal residual stress caused by a greater volume shrinkage in the drying process which reduces molecular mobility and, thus, reduces the hysteresis [57].

The BTO particles increased the magnitude of the hysteresis by simply increasing the overall capacitance of the material. The results also showed increased hysteresis, which correlates with the increase in the particle size of the filler material. This trend has been demonstrated in the literature, where it was showed that well-dispersed polymer–filler systems have a significantly larger dynamic modulus phase angle for larger particles (elastic materials have a phase angle of 0°, and viscous materials have a phase angle of 90°) [58]. Moreover, the phase angle magnitude in viscoelastic polymer–filler composites is more significantly influenced by agglomerations in the filler material than by the particle size [59]. Since the BTO particles, considered in this work to be 1 μm, were actually small agglomerations formed by sintering, they contributed greatly to this trend. The compositions with a higher volume content of ceramics showed decreased hysteresis at higher temperatures. This is in accordance with experimental results, which show that filler materials lower the magnitude of the viscoelastic spike in polymer–filler composites [60, 61].

It has been shown that the phase angle of the dynamic modulus peaks at 100 °C for PVDF, and at 120 °C for PVP, indicating a transition from a glassy state to a more viscous rubbery state [42, 62]. While it is known that reduced molecular weight polymers experience less hysteresis, this work showed that the sensor compositions with 50 vol% PVP (8000 g mol^{-1} MW)/50 vol% PVDF (500 000 g mol^{-1} MW) experienced higher hysteresis than those containing only the high molecular weight polymer PVDF. This effect is caused by an increase in the polydispersity, which decreased the viscosity of the polymer blend. This in effect increased the molecular mobility of the binder, giving rise to the overall hysteresis in the matrix [33, 34]. The materials with the MPTS modifier experienced higher hysteresis as the brush-like architecture of the modifier increased intermolecular interactions and increased various slip-links [30–32].

The increased modifier content decreased hysteresis in the sensors. Using the above-mentioned criteria to evaluate the effects of the modifier content, a number of mechanisms (i.e. polymer mobility, polydispersity, density) are found to promote and depress hysteresis. The exact mechanism causing the relationship between the modifier content and hysteresis could not be definitively determined.

4.7. Thermomechanical drift

The drift caused by the thermomechanical loading was affected by similar compositional and microstructural variables at both high and low temperatures—with the exception of thickness, which had negligible effect at low temperatures. At high temperatures, the drift was reduced in thicker films, as the thicker films are known to experience increased internal residual stress which suppresses the reorganization of the microstructure. As with hysteresis, the BTO particles increased the magnitude of the drift more than the inclusion of the PZT particles, by further increasing the overall capacitance of the materials.

Compositions with smaller particle sizes were found to exhibit higher drift. This is believed to be a function of the differences in the electrical properties of the materials. The composite materials consisting of conductive filler materials are shown to have non-Ohmic characteristics, caused by electron tunneling between the filler particles [63]. Electron tunneling from particle to particle through the bulk material was exponentially increased by reducing the inter-particle spacing, and the inter-particle spacing was linearly decreased by reducing the particle size. This was similarly found in other works [64]. Thus, reducing the particle size exponentially increased the effects of electron tunneling in

the polymer–filler composites, resulting in a reduction in the effective percolation threshold.

The compositions in this work do not include conductive fillers; however, ferroelectric particles produce a similar effect on the electrical flux of the composite. Rather than affecting conductivity, reduced inter-particle spacing was found to affect charging of the bulk material by increasing the electric flux [65, 66]. This causes compositions with smaller particles to experience greater changes in charging, as the effects of electrical flux are more significant. Additionally, smaller particles are more likely to be displaced in the composite microstructure, causing compositions to experience increased changes in the electric flux, making them more susceptible to cause drift. Drift was also more pronounced when less ceramic materials were used, as the composite is more heterogeneous and the particle shifting causes more severe changes in the electrical flux.

The molecular weight of the polymers directly affected the shifting and reorganization of the microstructure. It has been shown that polymers with a molecular weight near that of PVP (8000 g mol^{-1} MW) will wrap single surfactants, while high molecular weight polymers such as PVDF (500 000 g mol^{-1} MW) are found to bind multiple surfactants, creating a complex matrix [25]. Here we find a similar effect in the ceramic-filled polymer composites, which are known to contain agglomerated particles within the composite microstructure [26]. The result is small, simple aggregates forming within PVP matrix, and large, complex aggregates forming in the PVDF matrix. In this work, composites composed of the PVDF matrix showed aggregates in the range of 2 μm, as seen in figure 10. These more complex aggregates reduce reorganization of the microstructure, thus reducing drift. Another important contribution to drift is the addition or removal of residual stresses during reorganization of the softened microstructure during the thermomechanical process. The modifier MPTS is known to promote adhesion between polymers and, therefore, reduce drift over DEGBE modifier. The drift was further reduced by decreasing the content of the modifiers, which increased the mobility of the binder molecules.

4.8. Characterization of thermal affects on capacitance

The nonlinear dielectric character under thermal loading identified in this work was consistent with similar films tested by Furukawa *et al*. Smaller casting thicknesses increased the thermal drift, which is greatly influenced by changes in the crystalline structure [67]. It is believed that thinner composite films experience crystalline changes more quickly and more severely, influencing the response from the dynamic temperature sweep. Compositions containing BTO experienced a higher change in capacitance under thermal load (thermal drift), especially those with a smaller particle size. This correlates with the Curie temperature being in the center of the temperature scheme for 100 nm BTO particles, just outside the testing range for particles over 200 nm, and far outside the range for both PZT particle sizes [20, 46, 47, 54]. Also, compositions with a higher ceramic content displayed a higher thermal drift, as the ceramic particles are the main source of the drift.

The same polymer and modifier variables that were found to increase the baseline capacitance were also found to increase thermal drift. It is believed that the introduction of internal stresses resulting from thermal loading more significantly affected the variables that promote low residual stress. This is because the low stress compositions showed a greater change in their internal stress upon the introduction of thermal stresses.

5. Sensor design

Using the conclusions from this work, a robust ceramic/polymer composite sensor material can be engineered. This design considers not only the linear trends of the Taguchi analysis, but also takes into account the more complex trends found in the literature to affect the results of the testing matrix. The following statements summarize the key findings of this work.

- The thickness of the sensor should be minimized to increase the sensor response and simplify potential future incorporation into a secondary structure or mechanism. Reduction of the film thickness is limited by a loss in strength, as the sensors should be easily handled without being damaged. Disadvantages include increases in the drift magnitude.
- High dielectric ceramic materials should be evaluated by their dielectric constant, Curie temperature, and wetting characteristics. Moving the Curie temperature towards −80 °C will increase the low-temperature response of the sensors, while drawbacks of this approach include an increase in the temperature drift of the sensor. Increasing the Curie temperature well above the working range would reduce this temperature drift.
- The particle size of the ceramic materials will be partially determined by placement of the Curie temperature. Smaller particles will increase the capacitance by increasing the electric flux percolation. Additional considerations include decreasing the compressive modulus by decreasing the particle size, without significantly increasing drift caused by reorganization of nano-particles in the microstructure.
- The ideal volume content of ceramic materials is most heavily influenced by its relation to the sensor response through its effects on the dielectric constant and modulus of the bulk material. These variables are optimized near a 10 vol% loading of the ceramic materials (for this particle size range).
- A polymer/modifier matrix should be selected with a melting temperature exceeding the thermal range of the application. Maintaining the elastic properties of the matrix throughout the required thermal range will eliminate hysteresis. The matrix should also have a low modulus, a high molecular weight, and a complex molecular architecture to reduce drift, while meeting ASTM E595 outgassing standards.

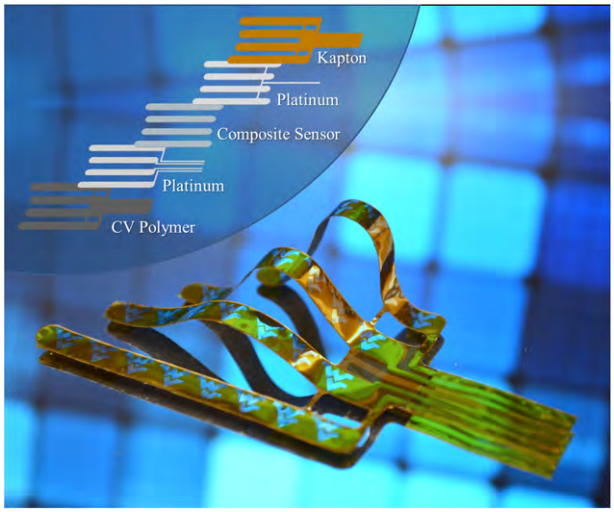

Figure 17. Sensor prototype fabricated to demonstrate use of the proposed smart film technology.

Design of the final sensor package and embedding technique into other structures should be considered during processing of the sensor composition. The sensor package, including electrodes and insulating coatings, should be thin, flexible, and similarly resistant to thermal effects. While variations in sensor packaging are infinite, one example is shown in figure 17. This sensor package was fabricated on a Kapton film substrate, having a 10 μm thick composite sensor composed of materials including Huntsman controlled volatility polymers and PZT. Platinum electrodes were used to prevent oxidation of the nano-foil. The complete sensor package has thickness of 50 μm.

6. Conclusions

In this work, a two-level Taguchi experimental design was used to prepare a test matrix, evaluating the effects of seven different compositional variables on a ceramic/polymer microstructure and sensor response. While the two-layer design is limited by linear trends in the results, the mechanisms affecting the results were evaluated from the literature and the nonlinear trends were presented and discussed. A material selection criterion was described for the proper sensor composition for future sensor package designs concerning embedded force/tactile sensors for harsh environment applications. The work showed that the sensor response was maximized by reducing the film thickness, increasing the dielectric constant, and decreasing the compressive modulus. These goals are optimized with high dielectric ceramics using a volume loading in the region of 10%, and matrix materials with molecular architectures which promote the introduction of compressive strain. The negative effects of drift can be minimized by increasing the sensor thickness, increasing the ceramic particle size, using matrix materials with a high molecular weight and a complex molecular architecture, and by the introduction of residual stress in the films. At high temperatures, a rate-dependent hysteresis was found to occur due to increased molecular mobility of the polymer matrix. This can be prevented by selecting polymers with transition temperatures further outside the operating temperature range.

Acknowledgments

The research was funded by a Grant from NASA Goddard Space Flight Center to WVU titled, ‘National Center for the Robotic Servicing of Orbital Space Assets’, contract number NNX10AD17A. Microscopy and clean room procedures were performed with support from the West Virginia University Shared Facilities. Dynamic mechanical analysis experiments were performed with assistance from Professor Dave DeVallance, in the West Virginia University Davis College of Agriculture, Natural Resources and Design. Electrical and thermal characterizations were carried out with the support of the Penn State User Research Facilities with assistance from Jeff Long and Rudeger Wilke. PZT materials were donated by Piezo Kinetics Incorporated, Bellefonte, PA.

References

[1] 2011 Federal Aviation Administration *2011 Commercial Space Transportation Forecasts*
[2] Ellery A, Kreisel J and Sommer B 2008 The case for robotic on-orbit servicing of spacecraft: spacecraft reliability is a myth *Acta Astronaut.* **63** 632–48
[3] National Aeronautics Space Administration 2013 *NASA facts Robotic Refueling Mission* (Greenbelt, MD: NASA GSFC)
[4] Bluethmann W, Rehnmark F, Nguyen T and Aldridge H 2001 Cooperative manipulation test bed: a facility for space robot control system development *Proc. 6th i-SAIRAS* (Quebec: Canadian Space Agency)
[5] Rehnmark F, Bluethmann W, Mehling J, Ambrose R O, Diftler M, Chu M and Necessary R 2005 Robonaut: the ‘Short List’ of technology hurdles *Computer* **38** 28–37
[6] Helmick D, Okon A and DiCicco M 2006 A comparison of force sensing techniques for planetary manipulation *Aerospace Conf.* (Piscataway, NJ: IEEE) pp 1–14
[7] Cheung E, Manzo M and McConnell R 1991 Using capaciflectors for ORU docking *Proc. from the 3rd Ann. Conf. on Intelligent Robotic Systems for Space Exploration* (Piscataway, NJ: IEEE) pp 76–80
[8] Fricke S, Friedberger A, Seidel H and Schmid U 2012 A robust pressure sensor for harsh environmental applications *Sensors Actuators* A **184** 16–21
[9] Ishihara T, Sekine M, Ishikura Y, Kimura S, Harada H, Nagata M and Masuda T 2005 Sapphire-based capacitance diaphragm gauge for high temperature applications *TRANSDUCERS’05. The 13th Int. Conf. on Solid-State Sensors, Actuators and Microsystems, 2005. Digest of Technical Papers* (Piscataway, NJ: IEEE) vol 1, pp 503–6
[10] Murphy D G and Deacon S A 2011 Manned GEO satellite servicing mission environmental effects measurements study *NASA Report* pp 1–63 (Hampton, VA: NASA Langley Research Center)
[11] Petkov M 2003 The effects of space environments on electronic components *NASA JPL Report* pp 1–28
[12] Vecchi F, Freschi C, Micera S, Sabatini A M, Dario P and Sacchetti R 2000 Experimental evaluation of two commercial force sensors for applications in biomechanics and motor control *5th Ann. Conf. of Int. FES*

[13] Yousef H, Boukallel M and Althoefer K 2011 Tactile sensing for dexterous in-hand manipulation in robotics—a review *Sensors Actuators* A **167** 171–87

[14] Wang S Y 2004 A finite element model for the static and dynamic analysis of a piezoelectric bimorph *Int. J. Solids Struct.* **41** 4075–96

[15] Puers R 1993 Capacitive sensors: when and how to use them *Sensors Actuators* A **37** 93–105

[16] Ashruf C M A 2002 Thin flexible pressure sensors *Sensor Rev.* **22** 322–7

[17] Brignell J E, White N M and Cranny A W J 1988 Sensor applications of thick-film technology *IEEE Proc.* I **135** 77–84

[18] Arshak K I, McDonagh D and Durcan M A 2000 Development of new capacitive strain sensors based on thick film polymer and cermet technologies *Sensors Actuators* A **79** 102–14

[19] Newnham R E, Skinner D P and Cross L E 1978 Connectivity and piezoelectric-pyroelectric composites *Mater. Res. Bull.* **13** 525–36

[20] Sun W 2006 Size effect in barium titanate powders synthesized by different hydrothermal methods *J. Appl. Phys.* **100** 83503

[21] Dietze M and Es-Souni M 2008 Structural and functional properties of screen-printed PZT–PVDF-TrFE composites *Sensors Actuators* A **143** 329–34

[22] Kobayashi Y, Kosuge A and Konno M 2008 Fabrication of high concentration barium titanate/polyvinylpyrrolidone nano-composite thin films and their dielectric properties *Appl. Surf. Sci.* **255** 2723–9

[23] Wang Y G, Zhong W L and Zhang P L 1994 Size effects on the Curie temperature of ferroelectric particles *Solid State Commun.* **92** 519–23

[24] Jaccard C, Kanzig W and Peter W 1953 Das Verhalten von kolloidalen Seignetteelektrika I, Kaliumphosphat KH_2PO_4 *Helv. Phys. Acta* **26** 521–44

[25] Mészáros R, Varga I and Gilányi T 2005 Effect of polymer molecular weight on the polymer/surfactant interaction *J. Phys. Chem.* B **109** 13538–44

[26] Teoh M M and Chung T S 2009 Micelle-like macrovoids in mixed matrix PVDF-PTFE hollow fiber membranes *J. Membr. Sci.* **338** 5–10

[27] Yang M H, Hou S Y, Chang Y L and Yang A M 2006 Molecular recoiling in polymer thin film dewetting *Phys. Rev. Lett.* **96** 066105

[28] Shaw T M, Suo Z, Huang M, Liniger E, Laibowitz R B and Baniecki J D 1999 The effect of stress on the dielectric properties of barium strontium titanate thin films *Appl. Phys. Lett.* **75** 2129–31

[29] Devonshire A F 1954 Theory of ferroelectrics *Adv. Phys.* **3** 85–130

[30] Rouse P E Jr 1953 A theory of the linear viscoelastic properties of dilute solutions of coiling polymers *J. Chem. Phys.* **21** 1272–80

[31] Lin Y H 1987 Number of entanglement strands per cubed tube diameter, a fundamental aspect of topological universality in polymer viscoelasticity *Macromolecules* **20** 3080–3

[32] Dalnoki-Veress K, Forrest J A, De Gennes P G and Dutcher J R 2000 Glass transition reductions in thin freely-standing polymer films: a scaling analysis of chain confinement effects *Le J. Physique* IV **10** 221–6

[33] Wasserman S H and Graessley W W 1996 Prediction of linear viscoelastic response for entangled polyolefin melts from molecular weight distribution *Polym. Eng. Sci.* **36** 852–61

[34] Montfort J P, Marin G and Monge P 1986 Molecular weight distribution dependence of the viscoelastic properties of linear polymers: the coupling of reptation and tube-renewal effects *Macromolecules* **19** 1979–88

[35] Vollenberg P H T and Heikens D 1989 Particle size dependence of the Young's modulus of filled polymers: 1. Preliminary experiments *Polymer* **30** 1656–62

[36] Bao N, Shen L, Srinivasan G, Yanagisawa K and Gupta A 2008 Shape-controlled monocrystalline ferroelectric barium titanate nanostructures: from nanotubes and nanowires to ordered nanostructures *J. Phys. Chem.* C **112** 8634–42

[37] Suntako R, Laoratanakul P and Traiphol N 2009 Effects of dispersant concentration and pH on properties of lead zirconate titanate aqueous suspension *Ceram. Int.* **35** 1227–33

[38] Boutaleb S, Zaïri F, Mesbah A, Naït-Abdelaziz M, Gloaguen J M, Boukharouba T and Lefebvre J M 2009 Micromechanics-based modelling of stiffness and yield stress for silica/polymer nanocomposites *Int. J. Solids Struct.* **46** 1716–26

[39] Ji X L, Jing J K, Jiang W and Jiang B Z 2002 Tensile modulus of polymer nanocomposites *Polym. Eng. Sci.* **42** 983–93

[40] Fu S Y, Feng X Q, Lauke B and Mai Y W 2008 Effects of particle size, particle/matrix interface adhesion and particle loading on mechanical properties of particulate–polymer composites *Composites* B **39** 933–61

[41] Alam P 2010 A mixtures' model for porous particle–polymer composites *Mech. Res. Commun.* **37** 389–93

[42] Cassu S N and Felisberti M I 1999 Poly (vinyl alcohol) and poly (vinylpyrrolidone) blends: 2. Study of relaxations by dynamic mechanical analysis *Polymer* **40** 4845–51

[43] Linares A and Acosta J L 1997 Tensile and dynamic mechanical behaviour of polymer blends based on PVDF *Eur. Polym. J.* **33** 467–73

[44] Drzymala J and Wheelock T D 1995 *Air Agglomeration of Hydrophobic Particles* (Ames, IA: Iowa State Univ. of Science and Technology)

[45] Bechhoefer J, Deng Y, Zylberberg J, Lei C and Ye Z G 2007 Temperature dependence of the capacitance of a ferroelectric material *Am. J. Phys.* **75** 1046–53

[46] Jin B M, Kim J and Kim S C 1997 Effects of grain size on the electrical properties of $PbZr_{0.52}Ti_{0.48}O_3$ ceramics *Appl. Phys.* A **65** 53–6

[47] Ohno T, Suzuki D, Ishikawa K and Suzuki H 2007 Size effect for lead zirconate titanate nano-particles with PZT (40/60) composition *Adv. Powder Technol.* **18** 579–89

[48] Forsbergh P W Jr 1949 Domain structures and phase transitions in barium titanate *Phys. Rev.* **76** 1187–201

[49] Kinoshita K and Yamaji A 1976 Grain-size effects on dielectric properties in barium titanate ceramics *J. Appl. Phys.* **47** 371–3

[50] Buessem W R, Cross L E and Goswami A K 1966 Phenomenological theory of high permittivity in fine-grained barium titanate *J. Am. Ceram. Soc.* **49** 33–6

[51] Buessem W R, Cross L E and Goswami A K 1966 Effect of two-dimensional pressure on the permittivity of fine-and coarse-grained barium titanate *J. Am. Ceram. Soc.* **49** 36–9

[52] Arlt G and Hennings D 1985 Dielectric properties of fine-grained barium titanate ceramics *J. Appl. Phys.* **58** 1619–25

[53] Bell A 1984 Residual stress in BTO from temperature *Ferroelectrics* **54** 147–50

[54] Curecheriu L, Buscaglia M T, Buscaglia V, Zhao Z and Mitoseriu L 2010 Grain size effect on the nonlinear dielectric properties of barium titanate ceramics *Appl. Phys. Lett.* **97** 242909

[55] Pertsev N A, Zembilgotov A G, Hoffmann S, Waser R and Tagantsev A K 1999 Ferroelectric thin films grown on tensile substrates: renormalization of the Curie–Weiss law

and apparent absence of ferroelectricity *J. Appl. Phys.* **85** 1698–701

[56] Cowie J M G 1991 *Polymers: Chemistry & Physics of Modern Materials* (Bocca Raton, FL: CRC Press)

[57] Ree M, Chu C W and Goldberg M J 1994 Influences of chain rigidity, in-plane orientation, and thickness on residual stress of polymer films *J. Appl. Phys.* **75** 1410–9

[58] Robertson C G, Lin C J, Rackaitis M and Roland C M 2008 Influence of particle size and polymer–filler coupling on viscoelastic glass transition of particle-reinforced polymers *Macromolecules* **41** 2727–31

[59] Osman M A and Atallah A 2006 Effect of the particle size on the viscoelastic properties of filled polyethylene *Polymer* **47** 2357–68

[60] Priya L and Job J P 2002 Poly(vinylidene fluoride)/clay nanocomposites prepared by melt intercalation: crystallization and dynamic mechanical behavior studies *J. Polym. Sci.* B **40** 1682–9

[61] Bleach N C, Nazhat S N, Tanner K E, Kellomäki M and Törmälä P 2002 Effect of filler content on mechanical and dynamic mechanical properties of particulate biphasic calcium phosphate—polylactide composites *Biomaterials* **23** 1579–85

[62] El Mohajir B E and Heymans N 2001 Changes in structural and mechanical behaviour of PVDF with processing and thermomechanical treatments. 1. Change in structure *Polymer* **42** 5661–7

[63] Sichel E K, Gittleman J I and Sheng P 1978 Transport properties of the composite material carbon-poly (vinyl chloride) *Phys. Rev.* B **18** 5712–6

[64] Jing X, Zhao W and Lan L 2000 The effect of particle size on electric conducting percolation threshold in polymer/conducting particle composites *J. Mater. Sci. Lett.* **19** 377–9

[65] Dias C J and Das-Gupta D K 1996 Inorganic ceramic/polymer ferroelectric composite electrets *IEEE Trans. Dielectr. Electr. Insul.* **3** 706–34

[66] Newnham R E 1985 Ferroelectric composites *Japan. J. Appl. Phys.* **24** 16–7

[67] Furukawa T, Ishida K and Fukada E 1979 Piezoelectric properties in the composite systems of polymers and PZT ceramics *J. Appl. Phys.* **50** 4904–12